1 On the Improvement of Computational Efficiency of Smoothed Particle Hydrodynamics to Simulate
2 Flexural Failure of Ice
3
4 Jitapriya Das, Håvard Holm
5 Department of Marine Technology, Norwegian University of Science and Technology
6 Trondheim, Norway

7

8   ABSTRACT

9 The Finite Element Method (FEM) has been extensively applied to model failure of ice but suffers from

10 mesh distortion especially when fracture or fragmentation is involved. The Smoothed Particle

11 Hydrodynamics (SPH) method can avoid this class of problems and has been successfully applied to

12 simulate fracture of solids. However, the associated computational cost is increased considerably for SPH

13 simulations. Reducing the computational time without any significant decrease in accuracy is naturally

14 quite critical for SPH to be considered as an efficient numerical tool to simulate failure. Thus, the focus

15 of the present article was to investigate the feasibility of different approaches of domain decomposition,

16 mass scaling, time scaling and coupled SPH-FEM techniques to improve the computational resource

17 requirement. The accuracy, efficiency and limitations of each of these approaches were discussed and the

18 results were compared with analytical solution and four- point beam bending experiments. The results

19 drawn from the comparisons substantiate that domain decomposition, mass scaling and process time

20 scaling can be adequately used for quasi-static cases to reduce the CPU requirements as long as the

21 kinetic energy is constantly monitored to ensure that inertial effects are negligible. Furthermore, as the

22 computational time primarily depends on the number of discrete particles in a simulation, coupled SPH-

23 FEM method was identified as a viable alternative to reduce the simulation time and the results from

24 such coupled simulations seem to agree well with published experimental data. This study showed that

25 the proposed methods were not only able to emulate the failure mechanisms observed during

26 experimental investigations but also reduce the computational resource requirements associated with

27 pure SPH simulations, without any significant reduction in numerical accuracy and stability.

28

32

33

INTRODUCTION

Increasing exploratory and transportation activities in the Arctic and sub-Arctic regions have improved activity of vessels operating along the Northern Sea Route. These vessels are required to progress through level ice and this has consequently increased the demand of ice-capable ship designs. Also, ensuring adequate safety in the Arctic waters requires a thorough understanding of ice load and how ice deforms and fails. This knowledge is crucial to come up with efficient designs that will enable these vessels to operate competently in the harsh Arctic environment. As the ship's bow comes in contact with ice, the ice is crushed locally until the contact area is wide enough to induce bending failure. The material properties affecting this failure behavior are site-specific and depend on many factors including temperature, grain structure, grain size, salinity, brine volume, loading rate and mechanism of loading (Timco and O.'Brien 1994). These factors are best determined by in-situ tests even though the tests are quite difficult to conduct. The severe conditions of the Arctic and sub-Arctic regions demand innovative solutions as conducting such in-situ tests can become dangerous and time-consuming considering the low temperatures, prevailing darkness and harsh weather. Consequently, it would be advantageous to develop accurate numerical techniques that can not only predict the correct stresses and strains at failure but also simulate fracture patterns and fracture locations that correspond well with those reported in the literature.

The Finite Element Method (FEM) has been the preferred approach to model the complex failure behaviour and progressive deformation of ice. Varsta (1983) was the first to present a non-linear bending failure model of an ice wedge in FEM using a simplified Tsai-Wu criterion. Since, this model was not thoroughly compared with experiments its accuracy could not be determined correctly. The Tsai-Wu failure surface has also been used much later by Liu et al. (2011) to implement a pressure-dependent material model for ship-iceberg collisions. The first significant contribution in the field of ice-structure interaction came from Derradji-Aouat (2003), who developed a multi-surface failure model of saline ice to capture the complex failure mechanisms associated with ship-ice interaction. This failure model, which takes into account the impact of temperature, strain rate and loading direction on the material properties of ice, has been implemented into an explicit finite element program by Wang and Derradji-Aouat (2009). The major challenge in simulating such interactions has been to model the continuous failure process of ice. Kolari et al. (2009) presented an anisotropic continuum damage mechanics model to predict this continuous failure process by using a model update technique that updated and refined the finite element mesh to capture the progressive fracture more accurately.

Although FEM is used for failure analysis of ice, it is not able to predict the continuous failure mechanism satisfactorily as this introduces numerical difficulties caused by severe element distortion and negative volume problems. The problem can be resolved by introducing an erosion criterion, where the distorted elements are removed from the system based on a predefined failure criteria such as pressure, stress, strain, damage and temperature (Swaddiwudhipong et al. 2010). Erosion is essentially a numerical technique used in conjunction with FEM to predict fracture pattern, and the erosion parameters are generally derived empirically or using an ad-hoc approach. Thus, the focus has been to opt for more robust numerical techniques and has naturally paved the way for more innovative solutions. Gürtner (2009) presented the cohesive element approach used with FEM to predict the dynamic fracture of ice. This model required the knowledge of energy release rates of different fracture modes, which were derived heuristically so as to attain good correspondence with experimental results. SPH is another method that can successfully avoid these pitfalls found in FEM. The SPH particles inherently follow deformation and offer a natural transition from a continuum to a fragmented state (Stansby and Ma 2016). Anghileri et al. (2005) compared the applicability of three different numerical models of FEM, Arbitrary Lagrangian Eulerian (ALE) and SPH to simulate hailstone impact on aircrafts. It was found that the FEM model could realistically simulate the phenomenon only when the mesh distortion was not high, but the SPH method was extremely useful and showed a good correlation between numerical and experimental investigations. Carney et al. (2006) also used SPH to present a phenomenological failure model for high strain rate behaviour of ice. This model took into account different yield strengths in tension and compression, and strain rate sensitivity of ice. Although the results showed good correspondence with experiments from Kim and Kedward (2000) and Kim et al. (2003), the model required an equation of state and certain parameters that had to be derived empirically to comply with experimental solutions. Using Carney's material model, Keegan et al. (2013) simulated hailstone impact on the leading edge of a turbine blade with the SPH method. This work not only identified an accurate material model able to capture the phenomena but also a numerical tool capable of realistically simulating such an event. The SPH method is a viable alternative to traditional grid-based methods for simulating high-velocity impact problems, where distortions are quite high and using standard Lagrangian grids result in erroneous solutions.

However, for low-velocity impact simulations the capability of SPH is not well documented. Some relevant literature is available for deformation and fracture behaviour in rocks. Ice, like rock, shows similar failure characteristics especially under compression. Both the materials exhibit brittle behaviour

under high strain rates and ductile behaviour under low strain rates (Renshaw and Schulson 2001). Cleary and Das (2008) initially looked into the potential of SPH to model fracture of rocks and demonstrated its accuracy and applicability by comparing elastic and elastoplastic deformation cases with FEM simulations. Therein, it was concluded that brittle fracture of rocks under compression during low impacts could be modelled with good accuracy using SPH. Ma et al. (2011) further investigated the compressive fracture and crack propagation of heterogeneous rocks under uniaxial and biaxial compression. The material heterogeneity of rock was successfully modelled using the Weibull distribution law (Deb and Pramanik 2013). Under quasi-static conditions SPH has been successfully used to model, rocks. For other rock-like materials, Tang et al. (2013) identified the factors influencing their quasi-static analysis and therein concluded that with a suitable choice of the particle approximation of momentum equation and smoothing length, the SPH method could favourably simulate progressive failure of similar solids under compressive loads.

Das (2017) used the SPH method for simulating bending failure of ice. A parametric study was conducted to determine the correct formulation, particle density, smoothing length and scaling factor (to initial smoothing length) required for accurately simulating failure of ice using the SPH method. The article validated the SPH method for simulating linear elastic bending and was subsequently extended to model four-point bending failure of ice. However, the associated computational cost increased considerably. Based on the limitations within which the work was carried out, and the results, it was highlighted that reducing the computing time, without significantly affecting the accuracy was a salient criterion for SPH to be considered as an efficient tool for predicting failure. One way to improve the computational efficiency of SPH was to use a suitable alternative to the conventionally used Gaussian kernel function which is computationally expensive because of its infinite range. Ito (2008) used a kernel function with only even-order terms to simulate hypervelocity axisymmetric impact problems more efficiently and accurately. Parallel computing algorithms have also proved to be computationally very efficient for large-scale SPH simulations (Nishiura et al. 2015). Furthermore, hybrid SPH method of coupling Lagrangian Finite Volume Method (FVM) and SPH was also proposed by Barcarolo (2013) to improve the convergence order, accuracy and efficiency of SPH. Similar to the coupling between FVM and SPH, the hybrid method of SPH-FEM has also been proven to improve computational efficiency and accuracy while mitigating the core disadvantages of FEM related to failure simulation. Most of the work that was carried out using coupled SPH and FEM has been limited to fluid-structure interactions, high-velocity impacts and metal-cutting problems. Such coupled approaches in the field of ice failure are

127 not very well documented. Only recently, Kim (2014) briefly mentioned the coupled SPH-FEM

128 approach in the context of pressure area distribution during accidental collision of ice mass and steel

129 structures. The different SPH-FEM coupling methods (Johnson 1994), domain decomposition

130 (Lapoujade et al. 2014), time scaling (Villumsen and Fauerholdt 2008) and mass scaling (Olovsson and

131 Simonsson 2006) techniques are investigated in this paper to present their computational advantages and

132 capability to simulate bending failure accurately.

133 **METHODOLOGY**

134 SMOOTHED PARTICLE HYDRODYNAMICS

135 Smoothed Particle Hydrodynamics (SPH) is a mesh-free Lagrangian method that was first developed by

136 Gingold and Monaghan (1977) to study astrophysical phenomena. Since then the SPH method has

137 evolved and diversified from the initial idea to reach the desired degree of maturity required to simulate

138 complex engineering problems (Barreiro et al. 2016). Traditionally SPH has been applied for

139 simulations related to computational fluid dynamics (Colagrossi and Landrini 2003), ocean and coastal

140 engineering (Wei and Dalrymple 2016). In the field of solid mechanics Allahdadi et al. (1993) were the

141 first to introduce a three dimensional SPH code predicting the dynamic material response under shock.

142 The initial algorithm of SPH for strength of materials has been refined over the years to improve stability

143 as well as convergence and resulted in more widespread application of the method. In the SPH method

144 the problem domain is divided into a set of uniformly or randomly distributed discrete elements referred

145 to as particles. These particles not only act as interpolation points but also possess material properties

146 and interact with the external and internal forces. In the following section, the basic SPH formulations

147 are discussed briefly. For a more comprehensive description of the method the reader is referred to Liu

148 and Liu (2003).

149 *Integral representation of a function*

150 The integral representation of a function *f(x)* is written as:

$$f(x) = \int_{\Omega} f(x')\delta(x - x')dx' \tag{1}$$

151 where the problem domain is given by *Ω* and $\delta(x - x')$ is the Dirac delta function defined as:

$$\delta(x - x') = \begin{cases} 1 & x = x' \\ 0 & x \neq x' \end{cases} \tag{2}$$

152 *Kernel approximation of a function*

153 For the kernel estimate, the Dirac delta function is replaced by a smoothing function $W(x - x', h)$.

$$\langle f(x) \rangle = \int_{\Omega} f(x')W(x-x',h)\,dx' \tag{3}$$

154   The smoothing function $W(x-x',h)$ has a compact support domain proportional to the smoothing length

155   (h). The domain extends up to κh, where κ is a constant such that $W(x-x',h)=0$ when $|x-x'| \rangle \kappa h$ i.e. the

156   smoothing function is equal to zero when the particle lies outside the domain. This is also known as the

157   compact condition (Liu and Liu 2010). Consequently, the integration over the problem domain Ω can be

158   reduced to κh, the support domain of the kernel function as shown in equation (4):

$$\langle f(x) \rangle = \int_{0}^{\kappa h} f(x')W(x-x',h)\,dx' \tag{4}$$

159   *Smoothing function*

160   A general expression for the smoothing function is written as:

$$W(\boldsymbol{x},h) = \frac{1}{h(\boldsymbol{x})^a}\theta(\boldsymbol{x}) \tag{5}$$

161   where h is the smoothing length, a depends on the number of space dimensions and $\boldsymbol{x}$ is the location of

162   the particle (Hallquist 2006) .

163   Gingold and Monaghan (1977) in their first paper on SPH used a Gaussian kernel, which is given by:

$$\theta(d) = C \cdot \begin{cases} e^{-d^2} & 0 \le d < 3 \\ 0 & d > 3 \end{cases} \tag{6}$$

164   Here, C is the normalisation constant such that $C = \left[\dfrac{1}{\sqrt{\pi}}, \dfrac{1}{\pi}, \dfrac{1}{\pi^{3/2}} \right]$ in $[1D,\ 2D,\ 3D]$ to satisfy the

165   normalisation condition (Liu and Liu 2010); $d = r_{ij}/h$, r_{ij} is the distance between the particles i and j, h is

166   the smoothing length. However using such a kernel is computationally less efficient considering its

167   infinite range. More traditionally, for SPH simulations a cubic spline having a narrower support, as

168   shown in Figure 1, is often used. Such a function is defined by:

$$\theta(d) = C \cdot \begin{cases} 1 - \dfrac{3}{2}d^2 + \dfrac{3}{4}d^3 & 0 \le d \le 1 \\ \dfrac{1}{4}(2-d)^3 & 1 \le d \le 2 \\ 0 & d > 3 \end{cases} \tag{7}$$

169   For the cubic spline kernel $C = \left[\dfrac{2}{3}, \dfrac{10}{7\pi}, \dfrac{1}{\pi} \right]$ in $[1D,\ 2D,\ 3D]$
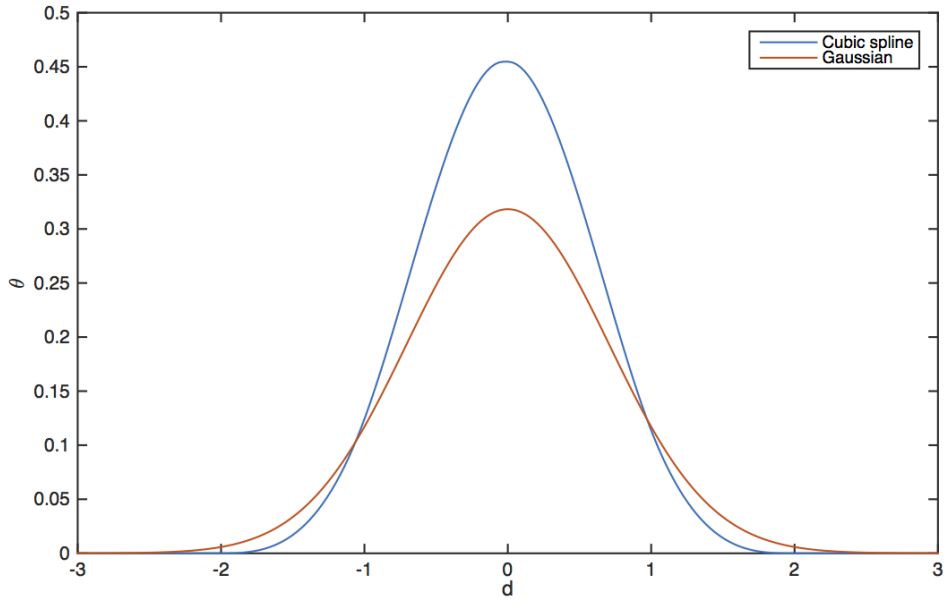
Figure 1: 2D form of cubic spline and Gaussian kernel

174

175 *Particle approximation*

176 The particle approximation of any field variable at a particular **SPH** node is carried out by substituting

177 the integral in the kernel approximation by a summation symbol which covers all the particles in the

178 support domain of the SPH node weighted by the kernel function. Figure 2 shows the neighbouring

179 particles in the support domain of particle *i*. The corresponding particle approximation of a field

180 function *f(x)* at particle *i* is written as:

181

$$\langle f(x_i) \rangle = \sum_{j=1}^{n} w_j f(x_j) \cdot W_{ij} \tag{8}$$

182 where $w_j = m_j / \rho_j$ and $W_{ij} = W(x_i - x_j, h)$

183

184

185

186

187

188
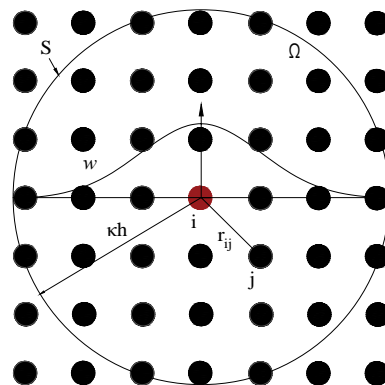
190   Figure 2: Particle approximation of particle i with support domain κh

191   The particle approximation of the spatial derivative of a function can be similarly expressed as

$$\langle \nabla . f(x_i) \rangle = \sum_{j=1}^{n} w_j f(x_j) \cdot \nabla_i W(x_i - x_j, h) \tag{9}$$

192   Equation (9) shows that the SPH approximation of the gradient of a field function requires the absolute

193   values of the function itself weighted by the gradient of the kernel function, which is shown in (10).

$$\nabla_i W(x_i - x_j, h) = \nabla_i W_{ij} = \frac{\partial W_{ij}}{\partial r_{ij}} \left[\frac{x_i - x_j}{r_{ij}} \right] = A_{ij} \tag{10}$$

194   where r_{ij}, is the distance between particles i and j

195   *Governing equations*

196   The balance laws of continuum mechanics, in the Lagrangian frame of reference, are given in equations

197   [(11)-(13)]. In the following equations d/dt indicates the total time derivative, α and β are the

198   coordinate directions and components with repeated indices are summed over.

199

200   i.   The continuity equation:

$$\frac{d\rho}{dt} = -\rho \frac{\partial v^{\beta}}{\partial x^{\beta}} \tag{11}$$

201   ii.   The momentum equation:

$$\frac{dv^{\alpha}}{dt} = \frac{1}{\rho} \frac{\partial \sigma^{\alpha\beta}}{\partial x^{\beta}} \tag{12}$$

202   iii.   The energy equation

$$\frac{de}{dt} = -\frac{P}{\rho} \frac{\partial v^{\alpha}}{\partial x^{\beta}} \tag{13}$$

203   Here ρ is the density, v^{α} is the velocity in α direction, $\sigma^{\alpha\beta}$ is the stress tensor, e represents the energy and

204   P is the pressure.

205

206   *Particle approximation of the governing equations*

207   i.   The continuity equation

208 For particle approximation of the continuity equation, the approximation is applied to the divergence

209 component of equation (11). The particle approximation of the continuity equation is written as:

$$\frac{d\rho_i}{dt} = -\rho_i \sum_{j=1}^{n} \frac{m_j}{\rho_j}(v_j^\beta - v_i^\beta)A_{ij} \tag{14}$$

210 It is also possible to derive various forms of particle approximation for the same conservation equation

211 by considering different identities. An alternative expression for the continuity equation is given by:

$$\frac{d\rho_i}{dt} = -\sum_{j=1}^{n} m_j(v_j^\beta - v_i^\beta)A_{ij} \tag{15}$$

212   ii.   The momentum equation

213 The momentum equation in (12) can be re-written as:

$$\frac{dv^\alpha}{dt} = \frac{\partial}{\partial x^\beta}\left(\frac{\sigma^{\alpha\beta}}{\rho}\right) + \left(\frac{\sigma^{\alpha\beta}}{\rho^2}\right)\frac{\partial\rho}{\partial x^\beta} \tag{16}$$

214 The particle approximation of this equation can be written as:

$$\begin{aligned}\frac{dv_i^\alpha}{dt} &= \sum_{j=1}^{n} \frac{m_j}{\rho_j}\left(\frac{\sigma_j^{\alpha\beta}}{\rho_j}\right)A_{ij} + \frac{\sigma_i^{\alpha\beta}}{\rho_i^2}(\sum_{j=1}^{n}\frac{m_j}{\rho_j}\rho_j A_{ij}) \\ \frac{dv_i^\alpha}{dt} &= \sum_{j=1}^{n} m_j\left(\frac{\sigma_j^{\alpha\beta}}{\rho_j^2}A_{ij} + \frac{\sigma_i^{\alpha\beta}}{\rho_i^2}A_{ij}\right)\end{aligned} \tag{17}$$

215 Since the gradient of a cubic spline is antisymmetric i.e. $A_{ij} = -A_{ji}$ we can write:

$$\frac{dv_i^\alpha}{dt} = \sum_{j=1}^{n} m_j\left(\frac{\sigma_j^{\alpha\beta}}{\rho_j^2}A_{ij} - \frac{\sigma_i^{\alpha\beta}}{\rho_i^2}A_{ji}\right) \tag{18}$$

216   iii.   The Energy equation:

217 The energy equation can be re-written in the form of the continuity equation:

$$\frac{de}{dt} = -\frac{P}{\rho}\frac{\partial v^\alpha}{\partial x^\beta} = \frac{P}{\rho^2}\left(-\rho\frac{\partial v^\alpha}{\partial x^\beta}\right) = \frac{P}{\rho^2}\frac{d\rho}{dt} \tag{19}$$

218 Subsequently, the particle approximation of this form of the energy equation can be written using

219 equation (15):

$$\frac{de_i}{dt} = -\frac{P_i}{\rho_i^2}\sum_{j=1}^{n} m_j(v_j^\beta - v_i^\beta)A_{ij} \tag{20}$$

220 In SPH, the particle approximation is carried out at each time step and depends on the current local

221 distribution of the particles. However, it is necessary for computational reasons to keep the mass and

222 number of particles inside the influence domain unchanged. Thus, if M denotes the total mass of the

223 spherical influence domain, then to keep this total mass unchanged dM/dt must be zero and the

224   conservation of mass in (11) will require that the smoothing length is calculated as a function of the

225   divergence of velocity as shown in (21). This equation suggests that the number of neighbours inside the

226   influence domain will increase during expansion and decrease during compression. Moreover, the

227   number of particles inside the support domain has a direct consequence on the simulation result. If the

228   number is too small, the simulation is unable to simulate the interaction between the particles realistically

229   or if it is too large, the local properties of the particles are smoothed out thereby affecting accuracy.

$$\frac{dh}{dt} = \frac{1}{3}h \cdot div(v) \qquad (21)$$

230   In spite of the advantages that the SPH method offers, it suffers from certain disadvantages like lack of

231   consistency, tensile instability and reduced accuracy at the boundary. These inherent drawbacks can be

232   resolved by a combination of corrective measures best described in Swegle et al. (1995), Liu (2003) and

233   Lacome (2001). Apart from these drawbacks, the SPH is also less efficient computationally compared to

234   other traditional numerical methods. However, since it is based on the Lagrangian approach it can be

235   linked to a standard Lagrangian model like the FEM. Such linked (or coupled) models provide the

236   capability to carry out simulations involving both fracture and structural response at a reduced

237   computational cost (Johnson 1994).

238

239   SPH-FEM COUPLING TECHNIQUES

240   The FEM has been extensively used in the field of continuum mechanics for modelling continuous

241   matter (such as solids, fluids etc.). However, one of the most challenging aspects of FEM is its inefficient

242   handling of problems involving large deformation, fracture and fragmentation (Chen et al. 2013). If solid

243   elements are used to predict progressive fracture or deformation, excessive mesh distortion results in

244   zero or negative volume problems, which introduces numerical difficulties like premature termination.

245   To resolve this, the mesh-free approach of SPH can be used. This method successfully mitigates the

246   aforementioned disadvantages of FEM and is well suited for problems involving fracture or

247   fragmentation. However, one major drawback of SPH is the increase in computational resource

248   requirement. To optimize the computational cost, both SPH and FEM can be coupled. The SPH

249   method can be embedded within an existing FEM code by considering SPH particles as FEM nodes. In

250   SPH-FEM coupling, SPH particles are used in regions where fracture or deformation is likely to be

251   predominant, and FEM for discretizing the rest of the model. Such coupling not only helps in reducing

252   the computation cost, by decreasing the number of active SPH particles, but also helps in accurately

253   simulating fracture without the numerical instability found in FEM. Furthermore, the accuracy of the

254   analysis is also improved if the problem domain comprises solid elements tin addition to SPH particles

255   (Swaddiwudhipong et al. 2010).

256   An overview of the code structure for SPH and Lagrangian FEM provided in Johnson (1994) showed

257   that the major differences between the two methods involve only the calculation of strains, strain rates

258   and forces. Another important consideration is that the same material model can be used for both SPH

259   particles and finite elements. Thus, it was possible to combine both the methods with appropriate

260   conditions enforced at the SPH-FEM interface. At this SPH-FEM interface, the particles are constrained

261   and moved with the elements. The interface also ensured continuous bonding between the two methods.

262   In Figure 3 the particle "i" includes both finite elements (marked in green) and SPH particles in its

263   influence domain. Certain considerations are required in the way computations are carried out for

264   particles at such interfaces. While determining the strain and strain rate at each SPH particle at the

265   interface, only the SPH nodes within the support domain are considered, whereas while calculating the

266   internal forces, contributions from both finite elements and particles inside the influence domain are

267   required to be included Johnson (1994). This coupling can be done using a tied contact algorithm or

268   using an adaptive coupling technique, both of which are discussed briefly in the following section.
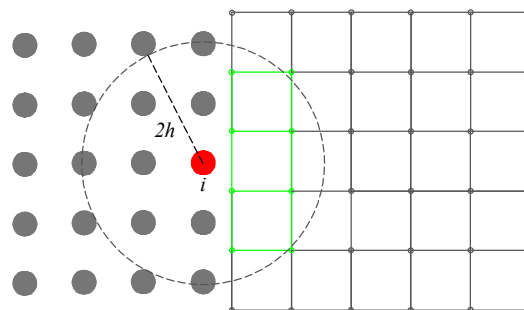
269   Figure 3: Coupling of SPH and FEM at the interface

270   *Tied contact*

271   A tied contact algorithm can be used to connect the SPH nodes with solid elements. Contact detection

272   algorithm requires a set of nodes called the slave nodes, and a set of surface patches called the master

273   surfaces to be defined (Attaway et al. 1994). During modelling, a node to surface contact was used with

274   the SPH particles as the slave nodes, and FEM elements at the interface as the master surface. During

275   initialization, all the slave nodes within the allowable standard projection from the master surface, was

276   tied and moved to the master surface to ensure zero gaps between FEM and SPH particles. Furthermore,

11

277   the displacement of the slave nodes was monitored throughout the calculation to check for penetration.

278   If the slave nodes penetrated the master surface, a contact constraint was applied to push back the slave

279   nodes on to the master surface. Instead of a tied contact, a tied offset contact could also be used. For

280   such contact algorithms, the slave nodes were not directly linked to the master surface. Rather, an offset

281   vector was defined at a specific distance from the master segment, and the slave (SPH) nodes were

282   connected to the end of this offset vector.

283
284   *Adaptive coupling method*

285   In FEM simulations fracture is often associated with numerical erosion of the failed element. This

286   erosion function is not a material property, but a numerical technique and is a very useful way to simulate

287   fracture. When an element is eroded its mass is either reduced to zero, which violates conservation of

288   mass, or is redistributed to the corner nodes. Nevertheless, both the compressive strength and the

289   internal energy of the eroded element are discarded (Kala et al., 2016). One way to solve this erosion

290   problem is to use adaptive coupling where the SPH elements replace the solid parts once they fail. The

291   activated SPH particle inherits all the mass, kinematic variables and constitutive properties of the failed

292   element.

293   In adaptive coupling, the SPH particles are included in the model from the beginning of a simulation.

294   However, they remain inactive until failure occurs so that the computational requirement is not

295   increased. Once failure occurs, the failed element is replaced by 1, 2 or 3 SPH particles. The inactive

296   SPH particles, at the start of a simulation, are marked in grey in Figure 4. Here, only one SPH particle is

297   placed at the centre of gravity of every element for representation. At the onset of failure, the failed

298   element is replaced by one SPH particle, marked in red in Figure 4(b). A contact interface, shown in

299   green, gets activated for the interaction between the undamaged FEM model and the activated SPH

300   particles (Kala and Hušek 2016).
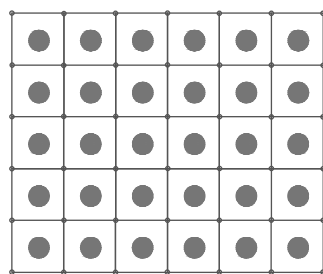
(a) Finite element mesh with SPH particles in the background   (b) SPH-FEM contact algorithm for adaptive coupling
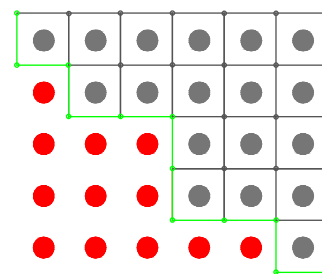
301

12

302   Figure 4

303   Although the SPH-FEM coupling is not entirely a new concept, the relevant literature on the efficiency

304   and applicability of such methods to simulate quasi-static phenomena is very limited. The outcome from

305   the numerical experiments are compared with the results of a series of four-point bending tests

306   conducted by Kujala et al. (1990) at the Gulf of Finland near Porkkala pilot station and serves as the basis

307   for comparing the efficiency and applicability of the numerical techniques presented in this article. The

308   experiment had a loading rig that was set up to ensure that bending took place upwards to bring about

309   tensile failure, which is the preferred mode of failure for ice going vessels. The loading rig had two

310   moving supports, spaced 1m apart, and was used to bend the beam against two fixed supports, spaced 4m

311   apart. A hydraulic cylinder, regulated by an electronically controlled pressure valve, produced the

312   bending force, which was measured by a force gauge attached to the hydraulic cylinder and linear

313   potentiometers measured deflection at each support and in the middle of the beam. The beams were

314   sawn from sea ice cover by a chainsaw to get straight edges. Furthermore, before conducting the tests,

315   surface temperature and dimensions of the beam were measured, and the loading rig was adjusted such

316   that the fixed top support of the loading platform and the upper surface of ice beams were at the same

317   level. The final deflection was calculated by subtracting the average displacement at the end supports

318   from the net deflection, measured at the middle of the beam and was considered necessary as the top

319   supports protruded slightly into the ice beam. The flexural strength values were about 24% higher

320   compared to results from (Enkvist 1972) and 30% higher values compared to Maattanen (1975). Also,

321   the elastic modulus determined from the experiments was found to be 5% to 20% greater than in

322   cantilever tests. In this article, the results from four-point bending simulations are compared with

323   experimental results from Kujala et al. (1990).

324   **NUMERICAL SIMULATION**

325   The numerical experiments are compared with the bending tests of natural sea ice conducted by Kujala

326   et al. (1990). Table 1 lists the properties of ice measured from the experiments.

327   Table 1: Material properties of Baltic Sea ice

| Elastic Modulus (E) (GPa)	Shear modulus (G) (GPa)	Bulk modulus (K) (GPa)	Density (ρ) (Kg/m³)	Poisson's ratio (ν)
4.154	1.562	4.073	917.12	0.33

328

329   Kujala et al. (1990) also presented a sensitivity study to determine how the Young's Modulus and the

330   flexural strength varied with temperature through the thickness of the ice beam. He assumed a linear

331   temperature gradient and constant salinity for the sensitivity study. Table 2 shows the calculated top (E)

332   and bottom elastic moduli (E') and the bending strength at the top surface (S). Here, F= load at failure, L

333   = distance between top supports and δ is the deflection.

Table 2: Calculated elastic moduli at top and bottom surface as well as bending strength

E (GPa)	α	E'(GPa)	S(MPa)
8.60	0.17	1.462	0.81

335

336   The SPH model of an ice beam in four-point bending had three parts viz. the sea ice beam, upper and

337   lower supports. The model is shown in Figure 5 where L, B and H denote the length, width and height

338   of the beam respectively. The measurements were directly taken from the in-situ beam bending

339   experiments. The SPH model had 702240 SPH nodes, and the supports were modelled as a rigid

340   material with 352 shell elements having an edge length of 0.05m. A penalty contact was required to be

341   defined to achieve contact between the rigid supports and the SPH ice beam (Hallquist 2006). The upper

342   support was fixed and the lower support was allowed to move in the Z-direction. The different colours in

343   Figure 5 indicate the different layers of the beam with varying material properties. A constant

344   displacement velocity (δ) was applied to the lower supports in the positive z-direction and this velocity

345   was calculated from full-scale test data.
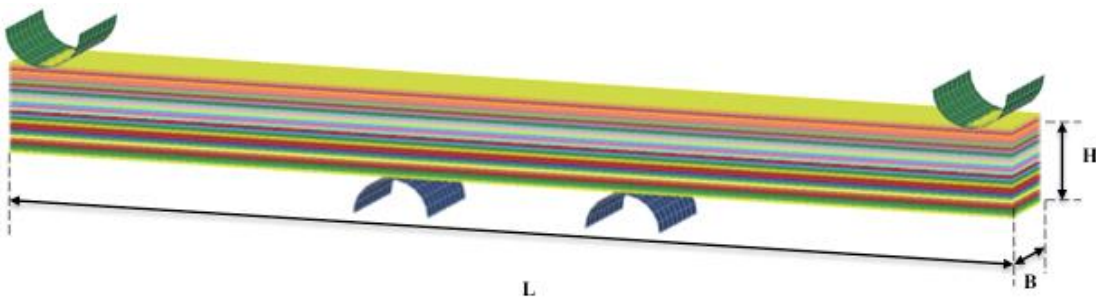
346

347   Figure 5: SPH model of an ice beam

348   MATERIAL MODEL

349   The experimental results showed only brittle elastic failure of the ice beams and consequently an elastic

350   failure model was selected. This model required the values of seven material parameters viz. density (ρ),

351   Shear Modulus (G), yield strength (σ_y), plastic hardening modulus (E_p), Bulk Modulus (K), pressure cut-

352   off (p_c) and failure strain (ε_f). Failure was specified either by the pressure cut-off (p_c) or failure strain (ε_f). At

353   the onset of failure, the deviatoric stress components were reduced to zero, and the material could only

354   carry compressive loads (Hallquist 2006).

355   The Von Mises yield criterion for the material is given by

$$\phi = J_2 - \frac{\sigma_{yield}^2}{3} \tag{22}$$

356   where J_2 is the second stress invariant and can be defined in terms of deviatoric stress components as

$$J_2 = \frac{1}{2} s_{ij} s_{ji} \tag{23}$$

357   The yield stress (σ_{yield}) is a function of effective plastic strain (ε_{eff}^p) and the plastic hardening modulus (E_p)

$$\sigma_{yield} = \sigma_0 + E_p \varepsilon_{eff}^p \tag{24}$$

358   The plastic hardening modulus (E_p) can be defined in terms of the tangent modulus (E_t) as

$$E_p = \frac{E E_t}{E - E_t} \tag{25}$$

359   The effective plastic strain is defined as:

$$\varepsilon_{eff}^p = \int_0^t d\varepsilon_{eff}^p \tag{26}$$

360   The pressure is given by equation (27), where K is the Bulk Modulus and V is the volume

$$p^{n+1} = K(\frac{1}{V^{n+1}} - 1); \tag{27}$$

361   The failure is assumed to occur if

$$p^{n+1} < p_c \text{ or } \varepsilon_{eff}^p > \varepsilon_f \tag{28}$$

362   where p_c and ε_f are user defined parameters.

363   In the experiment, the effective elastic modulus (E_{eff}) and bending strength were calculated from the

364   deflection. The flexural strength and elastic modulus depends on the temperature that varied through the

365   thickness of the beam. A linear temperature gradient and constant salinity was assumed Kujala et al.,

366   (1990) to present the variation of Young's modulus and flexural strength from the top to the bottom of

367   the beam. The plastic hardening modulus in Table 3 was assumed to be slightly lower than the elastic

368   modulus to differentiate between elastic and plastic behaviour. The yield strength was equal to the failure

369   stress at the top of the beam as shown in Table 3. Since it was preferred to initiate failure based on tensile

pressure, the failure strain (ε_f) was assumed to have a large value to not let the beam fail due to strain

371 criteria. The pressure cut-off value was taken from Soa (2011).

Table 3: Input values for the material model

ρ (kg/m3)	G (GPa)		σ_r (MPa)	E_e (GPa)		K (GPa)		p_c (MPa)
	Top	Bottom		Top	Bottom	Top	Bottom	
917.12	3.233	0.550	0.81	8.428	1.433	8.431	1.433	-0.2645

373

RESULTS AND DISCUSSION

The results from a parametric study of an SPH bar identified the correct formulation, number of particles, smoothing length and scaling factor (to the initial smoothing length) required to simulate tensile and compressive behaviour accurately using the SPH method (Das, 2017). Since beam bending includes both tensile and compressive stresses on either side of the neutral axis, this study was naturally extended to simulate four-point bending failure of an ice beam using SPH. In this study, the material properties of ice presented in Table 3 were used to simulate a FEM model of the same beam in four-point bending. Although the FEM is one of the most extensively used numerical tools in the field of solid mechanics, it suffers from a few limitations while simulating fracture or fragmentation. One such challenge is element distortion and a way to resolve this is through numerical erosion of solid elements. However, the capability of the finite element model to simulate the physical phenomena accurately depends on the correlation between the discretization length and the solid elements. Thus, such deletion of elements (or drop in mass) is a direct violation of the conservation of mass and is not preferred (Das et al., 2014). Besides, in an SPH analysis, no particles are removed from the problem domain at failure, and the mass remains constant throughout the simulation (as only the inter-particle connections fail and the particles are not removed from the problem domain). This is considered to be a notable advantage of SPH over FEM, especially in simulations where fracture processes play a dominant role. Furthermore, the comparisons of the FEM results with SPH also showed that the breaking location was similar in both the models. However, the fracture pattern from the SPH simulation appear more realistic because SPH offers a natural transition from a continuum state to a fragmented state at the point of failure (Stansby and Ma 2016). Once failure occurred, the deviatoric stresses in the SPH particles were reduced to zero and the particles only carried stresses in compression, displaying fluid-like behaviour. Such a solid-to-fluid

396 transition of the SPH particles was regarded as failure. In contrast, for FEM, such a transition state could

397 only be simulated by physically removing the elements from the model (erosion).

398 <center>Table 4: Comparison of SPH and FEM results</center>

METHOD	Failure load (kN)	Failure time (sec)	Deflection (mm)	CPU time (hrs)
Experiment[1]	5.69	0.34	1.07	–
SPH	5.98	0.34	1.16	27.10
FEM	5.56	0.34	1.16	2.500

399 1 (Kujala et al. 1990)

400 While these advantages of particle methods over traditional FEM for predicting fracture is quite clear,

401 one cannot overlook the computational demand of SPH considering that the FEM model was

402 significantly faster than SPH (Table 4). Therefore, this study looked into the different methods that could

403 be applied to reduce the CPU costs associated with an SPH simulation. The applicability of domain

404 decomposition, time scaling, mass scaling and SPH-FEM coupling techniques to improve the

405 computational efficiency were investigated. The results were compared with the experiments to

406 determine the error and the improvement in computational resource requirement. A satisfactory way to

407 present the accuracy of the investigated results were taken from Villumsen et al. (2008), where the

408 percentage differences in failure and displacement outputs were compared with experimental data.

409 However, it was not possible to formulate a generic answer for the acceptable percentage difference. It

410 was important to keep this as low as possible, but taking into consideration, the extreme conditions

411 prevalent in the Arctic, the measuring uncertainty of the mechanical properties of ice, and the accuracy of

412 the experimental setup, an error percentage of less than ten was considered to be satisfactory for the

413 present study.

414

415 DOMAIN DECOMPOSITION

416 The size of numerical models has been continually increasing in recent times, and it is now quite

417 common to handle models with several millions of elements/particles (computational nodes).

418 Consequently, there has been a growing demand for parallel and scalable computations through Shared

419 Memory Parallel (SMP) or Massively Parallel Processing (MPP). The SMP provides a parallel

420 architecture where a model is solved using multiple processors on the same machine. Naturally, the

421 processors share the hardware resources and operating system, and communicate through shared

422 memory. However, the SMP shows limited scalability for more than eight processors. For larger

423 problems, a more favourable option is the MPP that is a synchronized handling of a task by several

424 processors having their own set of hardware resources. The MPP capability of LS-DYNA uses a data-

425   partitioning algorithm that divides a given model into subdomains, each of which is assigned to a

426   particular processor. Every processor independently advances the solution for its subdomain until the

427   end of the time step after which the processors communicate through a Message Passing Interface (MPI).

428   For FEM, this communication only happens while updating the nodal displacements and forces.

429   Contrary to this, for SPH, the processors are additionally required to communicate with each other.

430   Firstly, during particle sorting, which determines the neighbour list in the sphere of influence of each

431   SPH particle. Secondly, during calculating strain rates. And thirdly while computing internal forces on

432   each SPH particle and its neighbours. Furthermore, in Lagrangian FEM, only the nodes that are located

433   at the boundary between decomposition subdomains govern the communication between processors.

434   However, for SPH, any particle having a neighbour in another subdomain will affect the communication

435   requirements. This means that the processors are required to communicate for every particle that is

436   located at a distance less than twice the smoothing length. Consequently, the communication

437   requirements for SPH are not only more frequent, but also the volume of data transferred between

438   processors is higher. Thus, the data partitioning algorithms of MPP can significantly affect the efficiency

439   of a given problem Lapoujade et al. (2014). In the present study, three different domain decomposition

440   methods were investigated by dividing the model along one of the three coordinate axes, viz. SLICE X,

441   SLICE Y and SLICE Z (Figure 6), to determine the most efficient partitioning algorithm for the problem

442   at hand.
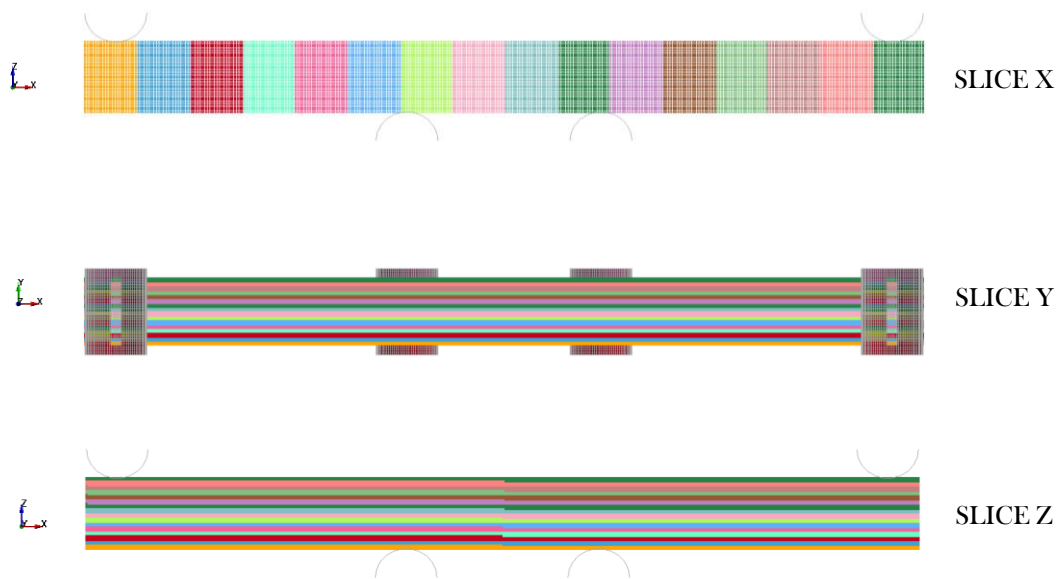
443   Figure 6: Different domain decomposition techniques

444   The load deformation response and fracture location for all the three decomposition techniques

445 correlated quite well. However, the computational efficiency for the three decomposition schemes

446 differed. Table 5 summarizes the results from the different decomposition schemes. SLICE X was

447 computationally most efficient and was 1.18 times faster than SLICE Y and 1.13 times faster than SLICE

448 Z. SLICE X has been used for all the numerical experiments presented hereafter in this article.

Table 5: Comparison of results for different decomposition schemes

Decomposition Scheme	Deviations in output at failure (%)		CPU time (hrs)
	Failure load	Displacement	
SLICE X	5.10	8.41	27.10
SLICE Y	5.10	8.41	31.88
SLICE Z	5.10	8.41	30.45

451 It is not surprising that the runtimes differ when the way a model is decomposed is changed. Each

452 processor, apart from the communication between them, also has to perform specific operations. If more

453 particles or computationally more expensive elements (due to material non-linearities or element

454 formulations) end up in one processor, it has to work harder. At the same time the remaining processors

455 have to wait till the end of each time cycle. There are a lot of different factors to consider when dividing

456 the problem into domains and it is challenging to determine, before the simulation is run, what the

457 optimal decomposition would look like since the deformation will affect the computational cost. Thus,

458 although the MPP takes advantage of better scaling and parallel capabilities through domain

459 decomposition and MPI, it is important to ensure that each processor has a good load balance between

460 them such that they are assigned at least several thousands of particles. Otherwise, the benefits of using

461 the MPP version will be quickly overshadowed by the communication requirements.

462

463 TIME SCALING

464 Time scaling is a technique that is used to reduce the simulation time by applying the given load more

465 quickly than in a quasi-static experiment. The study is applicable as long as the inertial effects are low and

466 the material behaviour is only slightly influenced by the corresponding strain rates. Two analyses, with

467 different time scaling factors of 2.5 and 5.0, were carried out to study its effect on the failure output.

468 For simulating the bending experiments, velocity boundary conditions were applied to the lower

469 supports. The velocities of the lower supports for each test were calculated from full-scale test data. For

470 time scaling, this applied velocity was artificially increased by factors of 2.5 and 5.0. The velocity profile

471 was defined by a half sine function curve that was gradually ramped up to the final scaled velocity. The

472 minimum ramp up time was set around 1.5-2.0 times the average period of the system to avoid inertial

473 effects that could change the response of the system (Hallquist 2006). The study was first conducted for a

474 linear elastic case for different time scaling factors of 2.5 and 5.0. The Normalised Root Mean Square

475 Error (NRMSE) was determined between the simulated forces and theory. For time scaling factors of 2.5

476 and 5.0, the NRMSE between the computed forces and analytical solution was 3.23% and 6.17%

477 respectively for linear elastic bending. The error percentage being within reasonable limits (below 10%

478 error is considered to be acceptable here), the study was subsequently applied to simulate four-point

479 bending failure of ice.

480 As shown in Table 6, using the time scaling technique significantly reduced the computation time. For

481 the analysis with a time scaling factor (TSF) of 2.5, the deviation in the load and displacement at the onset

482 of failure, compared to experimental results, were 4.39 and 7.48% respectively. At the same time the

483 CPU cost was reduced by 59%. The computation time was further reduced when the time scaling factor

484 (TSF) was increased to 5.0, and the corresponding difference in force and displacement outputs at failure

485 with experiments were 2.64% and 5.61% respectively. However, inertia effects slowly came into play as

486 evident from the abrupt spikes in the load-deformation curve for TSF = 5.0 (Figure 7). The abrupt

487 changes or fluctuations in the reaction forces (Figure 7) were caused because of the increasing loading

488 velocity, which caused higher reaction forces and possible penetrations at the contact interface between

489 the indenter (lower support) and the SPH ice beam, due to faster movement of the lower

490 supports/indenters. In this study, a penalty-based contact was defined between the supports and the

491 beam. For such contact definition, if a penetration was found (in this case the lower support penetrated

492 into the ice beam because of the higher velocity), a force directly proportional to the penetration depth

493 was applied to resist and eventually eliminate the penetration. Such elimination often caused oscillations

494 in contact responses, and is primarily responsible for the fluctuations in the load-deformation curve. A

495 damping coefficient can reduce such oscillations form penalty contacts. However, contact damping was

496 not used in the present study to ensure that the contact definition for all the numerical experiments

497 presented here was consistent. It can also be seen in Table 6 that the deviations in the output at failure

498 decreased, when compared to experiments, as the time scaling factor was increased. That said, with the

499 increase in time scaling, inertial effects caused higher reaction forces and stresses (pressure) within the

500 beam. Since a pressure-based failure criterion was used, the time-scaled models (TSF = 2.5 and TSF =

501 5.0) failed earlier and at a lower load and displacement levels than the SPH model with no time scaling

502 (TSF = 1). Thus, as the SPH model with TSF =1 gave higher failure results (about 5%) compared to

503 experiments, the failure outputs for the time-scaled models appear to be more accurate and closer to the

504 experimental investigations in Table 6. A better basis of comparison for the time scaling study would

505 have been the reference model of SPH-40 with no time scaling (TSF = 1), which would have showed that

506 the accuracy decreased with the increase in TSF. However, this was not done to be consistent with the

507 other results presented in the manuscript.

508

Table 6: Comparison of results for different time scaling factors

Time scaling factor (TSF)	Deviations in output at failure (%)		CPU time (hrs)
	Failure load	Displacement	
TSF = 1.0	5.10	8.41	27.10
TSF = 2.5	4.39	7.48	11.24
TSF = 5.0	2.64	5.61	5.080

509
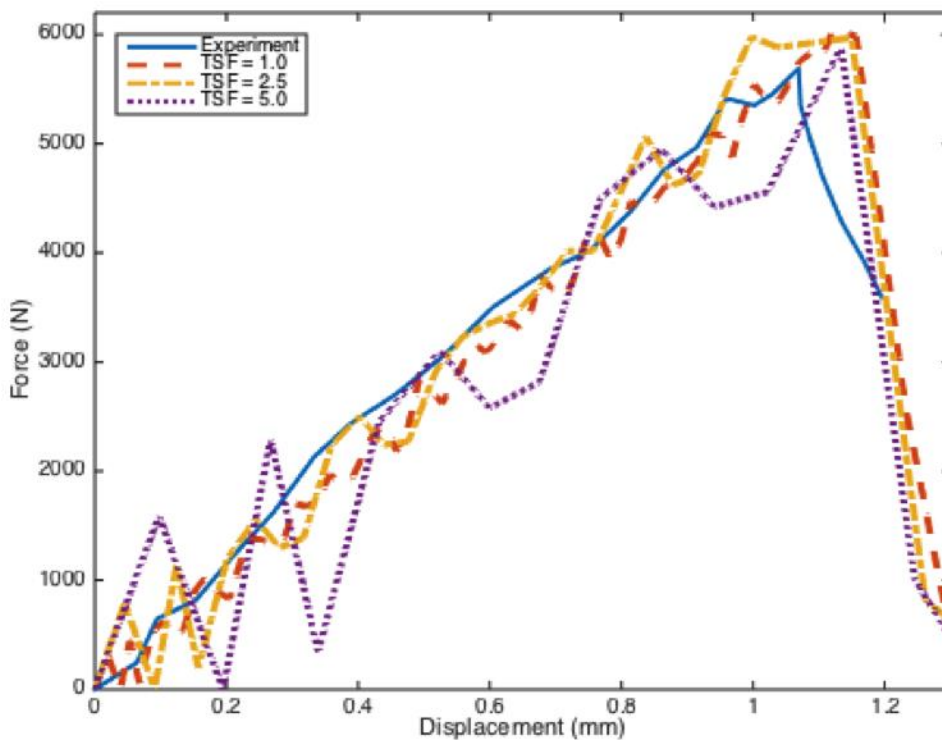
510

511 Figure 7: Force versus deflection plots for different values of process time scaling

512 Considering the computational demand of an SPH simulation and the improvement offered by

513 increasing the loading velocity, invoking time scaling was an efficient way to determine the results within a

514 reasonable timeframe. However, in a quasi-static experiment the load is applied very slowly such that the

515 structure deforms at a very low strain rate, and consequently the inertial forces can be ignored.

516 Therefore, if time scaling was used for a quasi-static case, it was important to check that the inertial effects

517 were minimal. To ensure this, the total kinetic energy had to be small compared to the total internal

518 energy of the system, during the simulation (for the models presented here, the total kinetic energy was

519 about 1% of the total internal energy, at the onset of failure). Also, the force-displacement response had

520   to be independent of the applied velocity. Based on the results from the numerical experiments, a time-

521   scaling factor of 2.5 was recommended to adequately simulate the four-point bending failure of an ice

522   beam without any significant instability and inertial effects.

523

524   MASS SCALING

525   Mass scaling refers to a technique of reducing the computational cost in an explicit analysis by adding a

526   non-physical mass to the structure that increases the critical time step. In standard FEM, mass scaling is

527   often applied to reduce the computational cost for explicit quasi-static simulations Prior (1994). In such

528   an analysis, the time step is calculated internally not only to maintain numerical stability but also to

529   ensure that the stress waves cannot propagate more than the minimum element dimension in one time

530   step. This is referred to as the Courant condition and is expressed in (29)

$$\delta t \leq C_{CFL}\left[\frac{h}{c}\right] \tag{29}$$

531   The time step (δt) is a function of the particle spacing (h), sound speed (c), and a stability constant C_{CFL}

532   (Hallquist 2006).The sound speed (c) depends on the element type and in its simplest form can be

533   written as $c = (E/\rho)^{\frac{1}{2}}$, where E is the Young's' Modulus and ρ is the material density. The internally

534   calculated time step for SPH method is slightly modified and takes into account the particle velocity (v),

535   as reflected in (30).

$$\delta t = C_{CFL}Min\left\{\frac{h(i)}{c(i)+v(i)}\right\} \tag{30}$$

536   Amongst all the factors controlling the internally calculated time step in an SPH simulation, there are

537   three parameters that can be changed to improve the time step. Firstly, it follows directly from (30) that

538   increasing the mesh size or the element length (h) will increase the time step. This should affect the

539   accuracy, and a convergence study must be conducted prior to determine the optimal mesh size for a

540   given problem. Secondly, Young's Modulus is changed thus directly altering the stiffness of the model

541   and thereby affecting the accuracy. Thirdly, the density of certain critical elements, responsible for

542   bringing down the time step in a simulation, is increased. This is also referred to as mass scaling where a

543   minimum time step size is specified. If an element or particle is responsible for bringing down the time

544   step below the specified minimum value, its density is increased to meet the minimum time step

545   requirements. In this study mass scaling was applied with the expectation to increase the critical time step

546   and consequently reduce the run time

547 An accurate SPH solution requires uniform distribution of particles Lacome (2001). Naturally, for such a
548 uniform discretization there is no specific particle controlling the time step. Villumsen et al. (2008)
549 indirectly invoked mass scaling of SPH particles in a metal-cutting simulation by directly increasing the
550 density of particles to examine the effect on the final result. In this study, mass scaling was similarly
551 introduced by scaling the density of each particle by ratios of 1.05 and 1.10. Similar to the previous
552 numerical experiment on time scaling, mass scaling was first applied to an elastic four-point bending case.
553 The NRMSE from the analytical solution was 6.06% and 12.71% for mass scaling factors of 1.05 and
554 1.10 respectively. At the same time, the computation time was reduced by 8.34% and 15.24%
555 respectively. The simulations were subsequently extended to the four-point bending failure analysis. The
556 deviations of the results from experiments are presented in Table 7. It can be seen that for a mass scaling
557 factor of 1.05 the force and displacement outputs at failure deviated by 4.22% and 1.87% respectively,
558 and calculation time was reduced by 9%. From the results, it is evident that further increasing the mass
559 scaling factor would reduce both the CPU requirements and the accuracy. Considering a below 10%
560 deviation in output as satisfactory, a mass scaling factor of 1.05 can be adequately used to simulate the
561 overall behavior of the numerical model within a reasonable timeframe. In a quasi-static analysis, mass
562 scaling has been similarly used to increase the critical time step and consequently reduce the run time
563 (Olovsson and Simonsson 2006) Still, the kinetic energy of the system was required to be monitored
564 regularly to ensure that it remained quite small compared to the internal energy, and that inertial effects
565 did not come into play.

566 Table 7: Comparison of percentage difference in results for different values of mass scaling

Mass Scaling Factor (MSF)	Deviations in output at failure (%)		CPU time (hrs)
	Failure load	Displacement	
MSF = 1.00	5.10	8.41	27.10
MSF = 1.05	4.22	1.87	24.84
MSF = 1.10	9.84	2.80	22.97

567

568 SPH-FEM COUPLING

569 The computational time in an SPH simulation primarily depends on the number of discrete particles
570 present in the model. Thus, a viable alternative to reduce the simulation time was to reduce the number
571 of active SPH particles in a simulation. This was achieved by coupling the Lagrangian methods of SPH
572 and FEM. SPH-FEM coupling could be done either by using the adaptive transformation of failed solid
573 elements into SPH particles or by using an offset tied contact to connect the SPH and FEM parts. In
574 adaptive transformation, the new particles assumed the properties of the original finite elements and

575 similar to using a tied contact improved the computational times by reducing the number of active SPH

576 particles in the model.

577 However, it was important to determine the most appropriate SPH and FEM models to couple together

578 and the discretisation error had to be calculated a priori, both for the FEM and SPH parts. The

579 appropriate models were selected from the results of a convergence study conducted for both SPH and

580 FEM beams under four-point bending. The convergence study for SPH was already presented in Das

581 (2017). Therein it was concluded that the height of the SPH beam if discretized using 40 particles (SPH-

582 40) and consequently assigning this inter-particle distance (to ensure uniform particle distribution) for the

583 entire model, the Normalized Root Mean Square Error (NRMSE) was found to be less than 4%. A

584 similar convergence study for FEM indicated that the NRMSE for FEM-20 (the height of the beam was

585 discretized using 20 elements) was around 2.4%, and further reducing the element size to FEM-40 only

586 reduced the error to 2.2%. However, this small improvement in accuracy of FEM-40, compared to FEM-

587 20, came at a significant increase in computational requirements (Table 8). Thus, considering both the

588 CPU resource requirements and accuracy, FEM-20 and SPH-40 were considered to be the most

589 appropriate models to couple together.

590

Table 8: Comparison of NRMSE and CPU costs for different FEM models

METHOD	Output at t = 0.4 s		NRMSE (%)	CPU time (hrs)
	Load (KN)	Displacement (mm)		
FEM-5	5.25	1.14	16.6	0.04
FEM-10	6.68	1.33	3.40	0.10
FEM-20	6.81	1.34	2.40	1.75
FEM-40	6.90	1.35	2.20	14.0

591
592 FEM-X indicates that the height of the beam is discretised using "X" number of elements. For instance, FEM-20 denotes that the
height of the beam is discretized using 20 elements
593

594 The coupled SPH-FEM methods were first validated for linear elastic four-point bending, by comparing

595 the contact force histories and deflection results with analytical solution and then extended to simulate

596 four-point bending failure of an ice beam. Two different coupled models are discussed in this article and

597 shown in Figure 8. The adaptive model had 11600 elements modelled using eight-noded solid elements

598 and 742400 SPH nodes that are shown in blue colour. Each FEM element was replaced by two SPH

599 particles at the onset of failure, to keep the inter-particle distance in the adaptive model consistent with

600 the pure SPH model. For the tied model, SPH was used for the middle part of the beam where fracture

601 was likely to occur and FEM for the rest of the beam. An offset contact was used to tie the FEM and

602 SPH parts. Such a contact allowed the SPH particles to be tied to the end point of a vector, offset at a

603 specified distance from the master segment of FEM.

604   In Figure 8, both the adaptive model and tied SPH-FEM models are shown. The SPH-FEM models

605   were first validated for a linear elastic bending case that ensured the applicability of the coupled models

606   to simulate bending. Thereafter, the SPH-FEM models were applied to simulate the flexural behaviour

607   of ice in four-point bending.

608

ADAPTIVE

TIED
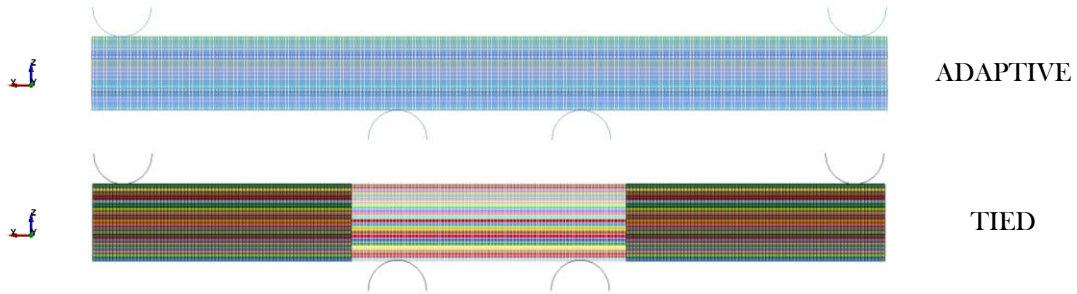
609   Figure 8: SPH-FEM coupling models

610   *Validation of SPH-FEM coupling techniques to simulate linear elastic bending*

611   The linear elastic bending results from the coupled SPH-FEM models were compared with FEM and a

612   pure SPH simulation of the same beam. For FEM analysis, the beam was modeled using the default

613   eight-noded solid element and the outcome from FEM was first matched with the analytical solution of

614   beam deflection under linear elastic bending. NRMSE further quantified the accuracy between the

615   numerical results and FEM. Although this normalised error percentage was least for the SPH method,

616   the adaptive model was the most efficient computationally (Table 9). Also, the NRMSE for the adaptive

617   model was only 0.47% more than the SPH method. This decrease was quite acceptable, especially

618   considering the significant improvement in efficiency.

619   Table 9: Comparison of linear elastic bending results between SPH and SPH-FEM models

METHOD	Output at t=0.4 s		NRMSE (%)	CPU time (hrs)
	Load (KN)	Displacement (mm)		
SPH-40	7.03	1.369	2.41	22.08
TIED	6.38	1.376	4.76	13.90
ADAPTIVE	6.79	1.354	2.88	2.170

620

621   Furthermore, the comparison of deflection (Figure 9) and load versus deformation plots (Figure 10)

622   between the coupled models, SPH and FEM, show good correlation between the different approaches

623   thereby contributing to the validation of the coupled models to simulate elastic bending behavior of ice.
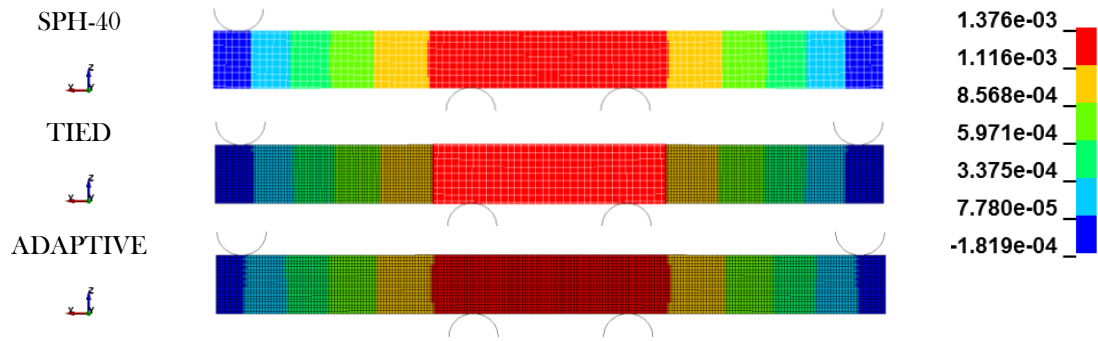
624

FEM

Deflection (m)

SPH-40

TIED

ADAPTIVE

1.376e-03
1.116e-03
8.568e-04
5.971e-04
3.375e-04
7.780e-05
-1.819e-04

Figure 9: Comparison of deflection at t = 0.40 s
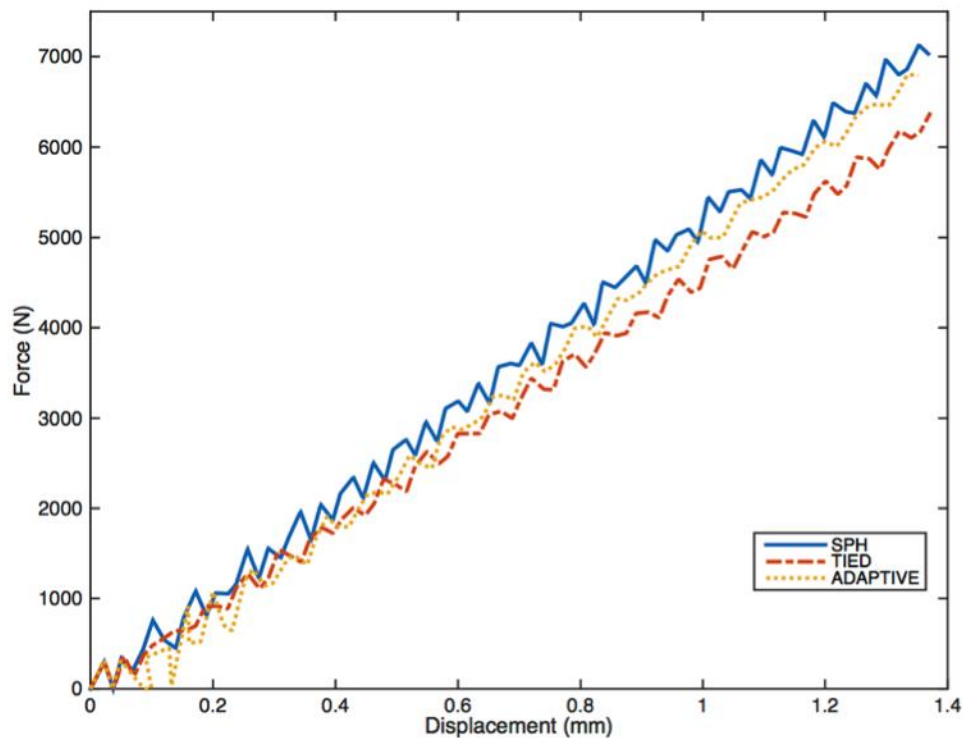

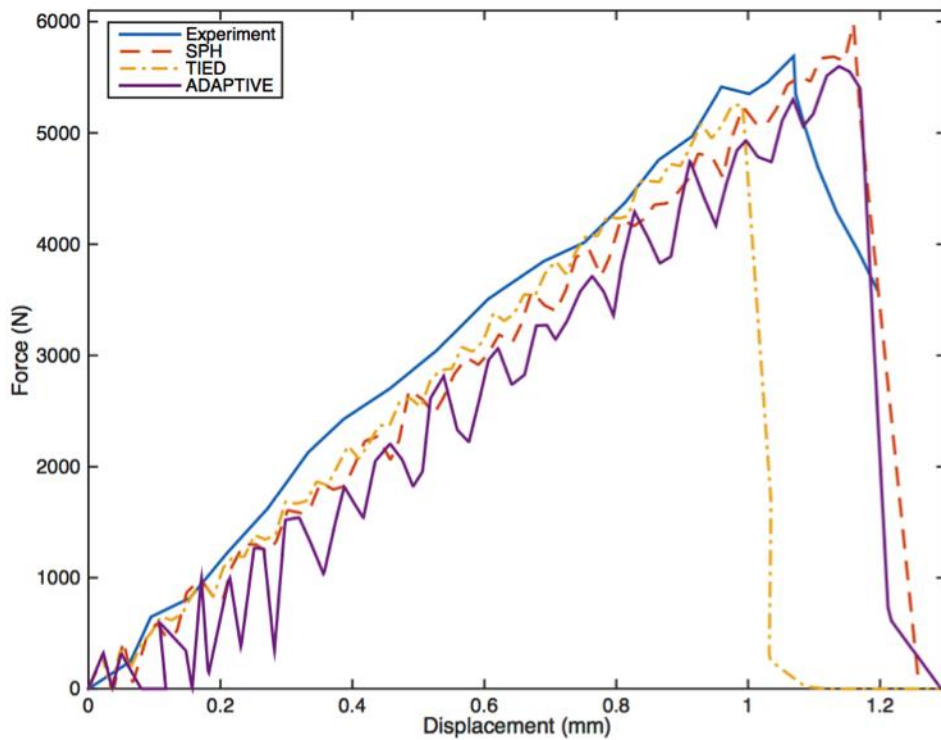Figure 10: Comparison of force-displacement plots between SPH and SPH-FEM models

Application of SPH-FEM coupling to simulate four-point bending failure of ice

The different coupling models were then used to simulate flexural failure of an ice beam under four-point bending. The outcomes from the numerical experiments are compared in Table 10. Both the adaptive and the SPH models agreed well with experimental results, particularly with respect to failure load, deflection and failure time. The force-displacement plots are compared in Figure 11. It can be observed that the tied contact model reached the tensile failure stress earlier than other numerical models. This is understandable because a tied contact connects two different domains and a discontinuity exists at the SPH-FEM boundary. The response in a tied contact was quite accurate initially. As the

26

638   deformation progressed, the stiffness, displacement, pressure and other key functionals started to be

639   different in the SPH and FEM parts leading to a dissimilar distribution around the tied interface. Prior to

640   failure, the distribution of tensile pressure in a few SPH elements at the tied interface was about twice the

641   surrounding solid elements and consequently led to premature failure there. Hence, a suitable solution

642   was to use the adaptive transformation of failed finite elements into SPH particles. For adaptive coupling,

643   such premature failure was not observed, and the failure results were found to be in good agreement with

644   experimental observations.

645
646   Figure 11: Comparison of force-displacement plots for SPH and SPH-FEM models

647   Table 10: Comparison of numerical results with experiment

METHOD	Deviations in output at failure (%)		Failure time (sec)	CPU time (hrs)
	Failure load	Displacement		
SPH-40	5.10	8.41	0.34	27.10
TIED	7.73	0.93	0.32	13.77
ADAPTIVE	2.46	8.41	0.34	4.730

648   _{1 (Kujala et al. 1990)}

649   The time requirement for the bending simulation can be substantially reduced if SPH-FEM coupling is

650   used instead of a pure SPH simulation. In fact, it can be seen from Table 10 that the tied model was two

651   times faster than SPH-40. However, variations in pressure distribution at the SPH-FEM boundary

652   initiated failure around the tied interface (Figure 12). The adaptive coupling model was almost six times

653 faster than a pure SPH simulation and the simulated failure load, time and displacement agreed well with

654 published experimental data.

655
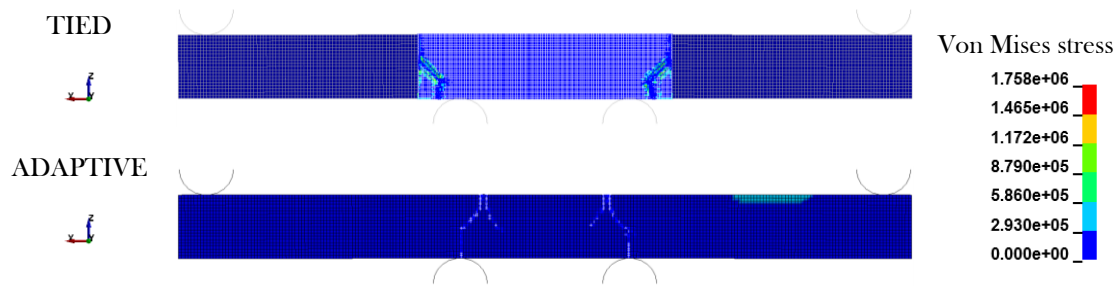
656 Figure 12: Breaking location and fracture pattern for SPH-FEM models

657

658 Table 11 reviews the different techniques studied in this paper and quantifies the reduction in

659 computational resource requirement and the associated error percentage compared to a pure SPH

660 model. The adaptive transformation of failed solid elements into SPH particles was computationally

661 most efficient. A combination of the described techniques can also be investigated to study the feasibility

662 of using them to improve the efficiency even more.

663 Table 11: Summary of results from domain decomposition, scaling techniques and SPH-FEM models

METHODS		Deviations in output at failure (%)		CPU time (hrs)
		Failure load	Failure displacement	
Domain Decomposition	SLICE X	5.10	8.41	27.10
	SLICE Y	5.10	8.41	31.88
	SLICE Z	5.10	8.41	30.45
Time scaling	TSF = 2.5	4.39	7.48	11.24
	TSF = 5.0	2.64	5.61	5.080
Mass scaling	MSF = 1.05	4.22	1.87	24.84
	MSF = 1.10	9.84	2.80	22.97
SPH-FEM	TIED	7.73	0.93	13.77
	ADAPTIVE	2.46	8.41	4.730

664

665

666

667

CONCLUSION

The SPH method, since its inception to simulate astrophysical phenomena, has gradually developed and diversified to become one of the best numerical methods to simulate fracture in brittle solids (Monaghan 2005). However, the computational requirements associated with SPH are significantly higher than conventional grid-based methods. Thus, several key ways to improve the computation time were investigated and their corresponding accuracy, ability to simulate failure, and limitations were compared. Of the key techniques investigated, domain decomposition, time scaling and mass scaling were found to be significantly useful to compute the results within a desired time limit. For quasi-static cases, these methods could be effectively used to reduce the CPU requirements by at least 59% for time scaling and 8% for mass scaling. At the same time, the corresponding deviations in output were less than 5% for failure load and 7.5% for failure displacement, when compared to experiments. These methods could provide valuable insights into the overall behaviour of a simulation as long as the kinetic energy was constantly monitored to ensure that inertial effects were negligible. The SPH-FEM models were also identified as viable alternative to significantly reduce the computational demand. If a tied contact was used to couple the SPH and FEM parts, the CPU requirements were reduced by almost 50%. However, the breaking location could not be simulated accurately in tied contacts as the discontinuity between the SPH and FEM parts resulted in premature failure at the contact interface. A suitable solution was to use adaptive transformation of failed finite elements into SPH particles. These new particles assumed the properties of the finite elements at failure, and not only improved the computational time by 83% but also the overall accuracy by 3%. The satisfactory correspondence of the simulation results with the experimental outcomes, especially with respect to failure load and displacement, confirm the accuracy and credibility of the different approaches presented in this paper. Future research should explore the application of these approaches in the context of combined bending and crushing failure of ice during ice-structure interactions.

REFERENCES

Allahdadi FA, Carney TC, Hipp JR, Libersky LD, Petschek AG (1993) High strain Lagrangian hydrodynamics: a three dimensional SPH code for dynamic material response. DTIC Document,

Anghileri M, Castelletti L-M, Invernizzi F, Mascheroni M (2005) A survey of numerical models for hail impact analysis using explicit finite element codes International Journal of Impact Engineering 31:929-944

Attaway S, Heinstein M, Swegle J (1994) Coupling of smooth particle hydrodynamics with the finite element method Nuclear engineering and design 150:199-205

Barcarolo DA (2013) Improvement of the precision and the efficiency of the SPH method: theoretical and numerical study. Ecole Centrale de Nantes (ECN)

Barreiro A, Crespo AJC, Dominguez JM, Garcia-Feal O, Zabala I, Gomez-Gesteira M (2016) Quasi-static mooring solver implemented in SPH Journal of Ocean Engineering and Marine Energy 2:381-396 doi:10.1007/s40722-016-0061-7

Carney KS, Benson DJ, DuBois P, Lee R (2006) A phenomenological high strain rate model with failure for ice International Journal of Solids and Structures 43:7820-7839

Chen H, Xu J, Wang C-H (2013) Hybrid element enabling solid/SPH coupling effect. Google Patents,

Cleary PW, Das R The potential for SPH modelling of solid deformation and fracture. In: IUTAM symposium on theoretical, computational and modelling aspects of inelastic media, 2008. Springer, pp 287-296

Colagrossi A, Landrini M (2003) Numerical simulation of interfacial flows by smoothed particle hydrodynamics Journal of Computational Physics 191:448-475 doi:http://dx.doi.org/10.1016/S0021-9991(03)00324-3

Das J (2017) Modeling and Validation of Simulation Results of an Ice Beam in Four-Point Bending Using Smoothed Particle Hydrodynamics International Journal of Offshore and Polar Engineering 27:82-89

Das J, Polić D, Ehlers S, Amdahl J Numerical Simulation of an Ice Beam in Four-Point Bending Using SPH. In: ASME 2014 33rd International Conference on Ocean, Offshore and Arctic Engineering, American Society of Mechanical Engineers.

Derradji-Aouat A (2003) Multi-surface failure criterion for saline ice in the brittle regime Cold Regions Science and Technology 36:47-70

Enkvist E (1972) On the ice resistance encountered by ships operating in the continuous mode of icebreaking.

Gingold RA, Monaghan JJ (1977) Smoothed particle hydrodynamics: theory and application to non-spherical stars Monthly notices of the royal astronomical society 181:375-389

Gürtner A (2009) Experimental and numerical investigations of ice-structure interaction. PhD thesis, Norwegian Uniersity of Science and Technology, Trondheim, Norway

Hallquist JO (2006) LS-DYNA Theory Manual Livermore Software technology Corporation, USA 3

Hallquist JO (2007) LS-DYNA keyword user's manual Livermore Software Technology Corporation 970

Ito R (2008) Computational Efficiency Improvements in Cylindrical SPH Analysis of Hypervelocity Impacts Japan Society of Aeronautical Space Sciences 56:407-415

Johnson GR (1994) Linking of Lagrangian particle methods to standard finite element methods for high velocity impact computations Nuclear Engineering and Design 150:265-274

Kala J, Hušek M (2016) Improved Element Erosion Function for Concrete-Like Materials with the SPH Method Shock and Vibration 2016

Keegan MH, Nash D, Stack M (2013) Numerical modelling of hailstone impact on the leading edge of a wind turbine blade EWEA Annual Wind Energy Event 2013

Kim E (2014) Experimental and numerical studies related to the coupled behavior of ice mass and steel structures during accidental collisions. PhD thesis, Norwegian Uniersity of Science and Technology, Trondheim, Norway

Kim H, Kedward KT (2000) Modeling hail ice impacts and predicting impact damage initiation in composite structures AIAA journal 38:1278-1288

Kim H, Welch DA, Kedward KT (2003) Experimental investigation of high velocity ice impacts on woven carbon/epoxy composite panels Composites Part A: applied science and manufacturing 34:25-41

Kolari K, Kuutti J, Kurkela J Fe-simulation of continuous ice failure based on model update technique. In: Proceedings of the International Conference on Port and Ocean Engineering Under Arctic Conditions, 2009. vol POAC09-104.

Kujala P, Riska K, Varsta P, Koskivaara R, Nyman T Results from in situ four point bending tests with Baltic sea ice. In: Helsinki University of Technology/Laboratory of Naval Architecture and Marine Engineering, IAHR Ice Symposium, Finland, 1990.

Lacome JL (2001) Smoothed particle hydrodynamics Livermore Software Technology Corporation, Livermore, CA

Lapoujade V, Mouteliere C, Millecamps A (2014) Advanced MPP Decomposition of a SPH Model 13th International LS-DYNA Users Conference

Liu GR, Liu MB (2003) Smoothed Particle Hydrodynamics: A Meshfree Particle Method. World Scientific,

Liu M, Liu G (2010) Smoothed particle hydrodynamics (SPH): an overview and recent developments Archives of computational methods in engineering 17:25-76

Liu Z, Amdahl J, Løset S (2011) Plasticity based material modelling of ice and its application to ship–iceberg impacts Cold Regions Science and Technology 65:326-334

Ma G, Wang X, Ren F (2011) Numerical simulation of compressive failure of heterogeneous rock-like materials using SPH method International Journal of Rock Mechanics and Mining Sciences 48:353-363

Maattanen M On the flexural strength of brackish water ice by in-situ tests. In: Proceedings of the POAC, 1975. pp 349-359

Monaghan JJ (2005) Smoothed particle hydrodynamics Reports on progress in physics 68:1703

Nishiura D, Furuichi M, Sakaguchi H (2015) Computational performance of a smoothed particle hydrodynamics simulation for shared-memory parallel computing Computer Physics Communications 194:18-32

Olovsson L, Simonsson K (2006) Iterative solution technique in selective mass scaling Communications in numerical methods in engineering 22:77-82

Prior AM (1994) Applications of implicit and explicit finite element techniques to metal forming Journal of Materials Processing Technology 45:649-656 doi:http://dx.doi.org/10.1016/0924-0136(94)90413-8

Renshaw CE, Schulson EM (2001) Universal behaviour in compressive failure of brittle materials Nature 412:897-900

Soa T (2011) Numerical Simulations of a Sea Ice Beam in Four-Point Pending. Master's thesis, Aalto University, Espoo, Finland

Stansby PK, Ma Q (2016) Foreword to special issue on particle methods for flow modeling in ocean engineering Journal of Ocean Engineering and Marine Energy 2:249-250 doi:10.1007/s40722-016-0065-3

Swaddiwudhipong S, Islamb M, Liu Z (2010) High velocity penetration/perforation using coupled smooth particle hydrodynamics-finite element method International Journal of Protective Structures 1:489-506

Swegle J, Hicks D, Attaway S (1995) Smoothed particle hydrodynamics stability analysis Journal of computational physics 116:123-134

Tang X, Zhou Y, Liu Y (2013) Factors influencing quasistatic modeling of deformation and failure in rock-like solids by the smoothed particle hydrodynamics method Mathematical Problems in Engineering 2013

Timco GW, O.'Brien S (1994) Flexural strength equation for sea ice Cold Regions Science and Technology 22:285-298 doi:http://dx.doi.org/10.1016/0165-232X(94)90006-X

Varsta P (1983) On the mechanics of ice load on ships in level ice in the Baltic Sea

Villumsen MF, Fauerholdt TG (2008) Simulation of metal cutting using smooth particle hydrodynamics Tagungsberichtsband Zum-DYNA Anwenderforum Bamb 30

Wang J, Derradji-Aouat A Implementation, verification and validation of the multi-surface failure envelope for ice in explicit FEA. In: Proceedings of the International Conference on Port and Ocean Engineering Under Arctic Conditions, 2009. vol POAC09-112.

Wei Z, Dalrymple RA (2016) Numerical study on mitigating tsunami force on bridges by an SPH model Journal of Ocean Engineering and Marine Energy Journal of Ocean Engineering and Marine Energy 2:365-380 doi:10.1007/s40722-016-0054-6